Calibration of a Polarimetric MIMO Array With Horn Elements for Near-Field Measurement

Lingyu Kong and Xiaojian Xu

***Abstract*— Polarimetric multiple input and multiple output (MIMO) radar is capable of acquiring target's high-resolution images and polarization scattering matrix (PSM). In this article, calibration of a polarimetric MIMO array of an instrumentation radar for near-field measurement is achieved at *X*-band by using a rotatable double-antenna polarimetric active radar calibrator (RODAPARC) and a metal cylinder quickly and accurately. The theoretical PSM of the RODAPARC with different antenna rotation angles is derived from Huygens' radiation electric field which is applicable to different bistatic angles. A polarimetric signal model is adopted to reduce the impact of the RODAPARC on calibration. Experimental studies are conducted on a polarimetric MIMO array which is measured and divided into quasi-monostatic and bistatic transceiver channels for assessment on the calibration performance. Promising calibration results are obtained with a polarization isolation improvement of about 16 dB and great reduction of the polarization channel gain error less than ±0.5 dB in amplitude and ±3° in phase. The calibrated polarization signatures for classic objects are consistent with the theoretical results.**

***Index Terms*— Multiple input and multiple output (MIMO) radar, polarimetric active radar calibrator (PARC), polarimetric calibration.**

I. Introduction

With the explosive development of multiple input and multiple output (MIMO) technology, more and more MIMO radars have been presented in [1]–[6]. MIMO is an enabling technique capable of imaging a target using only one snapshot [6], which is different from rail synthetic aperture radar (SAR) and turntable inverse synthetic aperture radar (ISAR). Polarimetric MIMO radar images the target rapidly, while also providing the polarization scattering matrix (PSM) of the target. Crosstalk and polarization channel gain error distort the receive signal in polarimetric radars. This distortion will be more serious for polarimetric MIMO radars in terms of multiple transceiver channels. Therefore, polarimetric calibration serves an important role in polarimetric MIMO radars.

According to the different polarimetric calibrators, polarimetric calibration can be divided into passive [7]–[9] and active [10]–[17] polarimetric calibration. The passive polarimetric calibrators involve corner reflectors, metal balls and cylinders, and so on. The polarimetric active radar calibrators (PARC) with adjustable radar cross section (RCS) are advantageous when compared with passive polarimetric calibrators with fixed RCS constrained by physical size and structure. The aircraft polarimetric SAR images was calibrated by PARCs and corner reflectors arranged in a cross shape [10]. The polarization modes of receive and transmit antennas of the PARC are orthogonal to each other, and three different PSMs of the PARC can be obtained by changing the rotation angle. In [11] and [12], the delay line is added to the transceiver circuit of the PARC, which separates the background from the target to improve the signal-to-noise ratio (SNR) of the receive signal. The PARC with independent rotatable double antenna was proposed in [15]–[17]. A variety of PSMs can be obtained by means of flexible combination of antenna polarization modes, which provides many options for polarimetric calibration methods.

Spaceborne- [11], [18], [19], airborne- [10], [20], and ground-based [21] polarimetric SAR must be calibrated to obtain the true information of the objects under study. Calibration techniques of polarimetric SAR usually are based on point targets [10], [11], [19]. Since the point targets with known PSM are only valid around them, a number of calibration targets need to be artificially deployed to achieve the calibration. To overcome the shortcomings of point targets, the polarimetric calibration techniques using distributed targets with good scene flexibility and adaptability, such as rainforest, grassland, and so on, were presented in [18], [20], [21]. Meanwhile, it is convenient to maintain and update the polarization characteristics of the system. However, almost all distributed target calibration methods require some assumptions, such as reciprocity [18], [20], [21] and reflection symmetry [22], [23].

Polarimetric MIMO radars have been seldom reported in the literature. It should be noted that in order to facilitate the analysis below, we define one transceiver channel including four polarization channels (HH, HV, VH, and VV) for polarimetric MIMO arrays. A polarimetric MIMO array with 16 transceiver channels applied for high precision direction of arrival estimation has been tested and calibrated in [24]. The array working at 77 GHz is very small, and the polarimetric calibration of all transceiver channels can be simplified to quasi-monostatic polarimetric calibration. An MIMO radar for near-field measurements [6] was fabricated in 2016, and it was upgraded to a polarimetric MIMO radar in 2017. There are two problems in polarimetric calibration of the array:

Manuscript received April 12, 2019; revised December 2, 2019; accepted January 14, 2020. Date of publication February 27, 2020; date of current version June 2, 2020. This work was supported in part by the Aeronautical Science Foundation of China (ASFC) under Grant 20162751012. *(Corresponding author: Xiaojian Xu.)*

The authors are with the School of Electronics and Information Engineering, Beihang University, Beijing 100191, China (e-mail: konglingyu@buaa.edu.cn; xiaojianxu@buaa.edu.cn).

Color versions of one or more of the figures in this article are available online at http://ieeexplore.ieee.org.

Digital Object Identifier 10.1109/TAP.2020.2975278

1) The polarimetric MIMO array has 80 transceiver channels, which greatly increases the complexity of polarimetric calibration.
2) The calibrator sensitive to bistatic angles cannot be used, such as dihedral and trihedral reflectors, because the polarimetric MIMO array has different bistatic angles in near-field measurement.

For the sake of bistatic polarimetric calibration, several solutions have been proposed in [25]–[28]. A polarimetric monostatic and bistatic RCS facility operating at W-band can be calibrated by a wire mesh with high cross-polarization level [25]. A unidirectional conducting canonical object has been introduced in [26], which satisfies the requirements as a cross-polarized bistatic calibration device. Due to their complex fabrication and fixed RCS, they can be applied to the RCS measurement system in anechoic chambers, but do not apply to the MIMO radar working outside because of nonadjustable RCS, especially not strong cross-polarization level. Mainlobe steered dihedral (MSD) object [27] with a high cross-polarization level can be applied for bistatic polarimetric calibration by adjusting the MSD design angles (ψ_{msd} and ϕ_{msd}) over a large range of bistatic angles. A PARC [28] with two Vivaldi antennas has been designed to accomplish polarimetric calibration by aiming the maximum beam direction of the PARC transceiver antenna at the bistatic RCS measurement radar. Since the polarimetric MIMO array has 80 transceiver channels, it is quite time-consuming and complicated for calibration of the polarimetric MIMO array by adjusting the MSD design angles or the maximum beam direction of the PARC transceiver antenna.

To calibrate the polarimetric MIMO array for near-field measurement quickly and accurately, we propose a polarimetric calibration procedure using a rotatable double-antenna polarimetric active radar calibrator (RODAPARC) [29] and a metal cylinder. The derivation based on Huygens' radiation electric field makes the PSM of the RODAPARC applicable to different bistatic angles. The quantitative information of all transceiver channels can be acquired by several snapshots of the polarimetric MIMO radar, rather than adjusting the maximum beam direction of the RODAPARC transceiver antenna for different bistatic angles, which greatly save the calibration time. Furthermore, a polarimetric signal model considering the RODAPARC is developed. Finally, a polarimetric MIMO array is calibrated by the propose procedure, and the expected calibration results can be obtained as the polarization isolation increased by approximately 16 dB and the polarization channel gain error less than ± 0.5 dB/$\pm 3°$.

II. Polarimetric Signal Model

Considering the background clutter, crosstalk, and polarization channel gain in a practical radar system, the polarimetric signal model can be expressed in the form of matrices as [9], [30]

$$\mathbf{M} = \mathbf{G} \odot \mathbf{RST} + \mathbf{I} \tag{1}$$

where $\mathbf{M}$ denotes the 2×2 measurement matrix and $\mathbf{I}$ refers to any undesirable signals (clutter, noise, interference, and so on). The 2×2 target scattering matrix $\mathbf{S}$ is mainly contaminated by the 2×2 polarization channel gain matrix $\mathbf{G}$, 2×2 transmitting distortion matrix $\mathbf{T}$, and 2×2 receiving distortion matrix $\mathbf{R}$. The operator $\odot$ represents a Hadamard product.

The relationship between the target scattering matrix and RCS is shown as

$$\sigma_{pq} = 4\pi R^2 |S_{pq}|^2 \tag{2}$$

where S represents the elements of the target scattering matrix, σ denotes RCS, R refers to the range, and the subscripts p and q are the normalized polarization vectors (H or V) for the receiver and transmitter, respectively.

Assuming that the SNR is high enough and the background clutter of the measurement environment can be well suppressed such that we can neglect the effect of $\mathbf{I}$ on the measurement, then (1) can be simplified as

$$\mathbf{M} = \mathbf{G} \odot \mathbf{RST} \tag{3}$$

with

$$\begin{bmatrix} M_{HH} & M_{HV} \\ M_{VH} & M_{VV} \end{bmatrix} = \begin{bmatrix} g_{HH} & g_{HV} \\ g_{VH} & g_{VV} \end{bmatrix} \odot \begin{bmatrix} R_{HH} & R_{HV} \\ R_{VH} & R_{VV} \end{bmatrix} \begin{bmatrix} S_{HH} & S_{HV} \\ S_{VH} & S_{VV} \end{bmatrix} \begin{bmatrix} T_{HH} & T_{HV} \\ T_{VH} & T_{VV} \end{bmatrix}. \tag{4}$$

Diagonalization of the receiving and transmitting distortion matrices is given by

$$\mathbf{R} = \begin{bmatrix} R_{HH} & R_{HV} \\ R_{VH} & R_{VV} \end{bmatrix} = \begin{bmatrix} R_{HH} & 0 \\ 0 & R_{VV} \end{bmatrix} \begin{bmatrix} 1 & \varepsilon_H^R \\ \varepsilon_V^R & 1 \end{bmatrix} \tag{5}$$

$$\mathbf{T} = \begin{bmatrix} T_{HH} & T_{HV} \\ T_{VH} & T_{VV} \end{bmatrix} = \begin{bmatrix} 1 & \varepsilon_V^T \\ \varepsilon_H^T & 1 \end{bmatrix} \begin{bmatrix} T_{HH} & 0 \\ 0 & T_{VV} \end{bmatrix} \tag{6}$$

where $\varepsilon_H^R, \varepsilon_V^R, \varepsilon_H^T$ and ε_V^T stand for the crosstalk parameters between the orthogonal polarization channels. Equation (3) can be rewritten as

$$\begin{bmatrix} M_{HH} & M_{HV} \\ M_{VH} & M_{VV} \end{bmatrix} = \begin{bmatrix} g_{HH} & g_{HV} \\ g_{VH} & g_{VV} \end{bmatrix} \odot \begin{bmatrix} O_{HH} & O_{HV} \\ O_{VH} & O_{VV} \end{bmatrix} \tag{7}$$

with

$$\begin{aligned} O_{HH} &= R_{HH}T_{HH}\left(S_{HH} + \varepsilon_H^R S_{HV} + \varepsilon_H^T S_{VH} + \varepsilon_H^R \varepsilon_H^T S_{VV}\right) \\ O_{HV} &= R_{HH}T_{VV}\left(\varepsilon_V^T S_{HH} + \varepsilon_H^R \varepsilon_V^T S_{HV} + S_{VH} + \varepsilon_H^R S_{VV}\right) \\ O_{VH} &= R_{VV}T_{HH}\left(\varepsilon_V^R S_{HH} + S_{HV} + \varepsilon_V^R \varepsilon_H^T S_{VH} + \varepsilon_H^T S_{VV}\right) \\ O_{VV} &= R_{VV}T_{VV}\left(\varepsilon_V^R \varepsilon_V^T S_{HH} + \varepsilon_V^T S_{HV} + \varepsilon_V^R S_{VH} + S_{VV}\right). \end{aligned} \tag{8}$$

A new point-wise product matrix can be constructed as

$$\tilde{G} = \begin{bmatrix} \tilde{g}_{HH} & \tilde{g}_{HV} \\ \tilde{g}_{VH} & \tilde{g}_{VV} \end{bmatrix} = \begin{bmatrix} g_{HH}R_{HH}T_{HH} & g_{HV}R_{HH}T_{VV} \\ g_{VH}R_{VV}T_{HH} & g_{VV}R_{VV}T_{VV} \end{bmatrix} \tag{9}$$

where $\tilde{g}_{HH}, \tilde{g}_{HV}, \tilde{g}_{VH}$, and $\tilde{g}_{VV}$ represent the polarization channel gain parameters. The polarization calibration model with 12 parameters can be simplified to 8 parameters polarization calibration model as

$$\begin{bmatrix} M_{HH} & M_{HV} \\ M_{VH} & M_{VV} \end{bmatrix} = \begin{bmatrix} \tilde{g}_{HH} & \tilde{g}_{HV} \\ \tilde{g}_{VH} & \tilde{g}_{VV} \end{bmatrix} \odot \begin{bmatrix} 1 & \varepsilon_H^R \\ \varepsilon_V^R & 1 \end{bmatrix} \begin{bmatrix} S_{HH} & S_{HV} \\ S_{VH} & S_{VV} \end{bmatrix} \begin{bmatrix} 1 & \varepsilon_V^T \\ \varepsilon_H^T & 1 \end{bmatrix}. \tag{10}$$

When the RODAPARC is applied in polarimetric calibration, its own crosstalk may be mistaken for the crosstalk of the radar system. This impact on calibration is usually negligible when the crosstalk of the RODAPARC is far below the crosstalk of the radar system. The crosstalk is mainly caused by the cross-polarization level of the antenna in the RODAPARC consisting of antennas, motors, and microwave devices. Our RODAPARC has the antenna with the cross-polarization level close to −40 dB, not the ultralow cross-polarization antenna. In order to obtain good calibration results, we introduce the crosstalk of the RODAPARC into the polarimetric signal model as follows:

$$\begin{bmatrix} M_{HH} & M_{HV} \\ M_{VH} & M_{VV} \end{bmatrix} = \begin{bmatrix} \tilde{g}_{HH} & \tilde{g}_{HV} \\ \tilde{g}_{VH} & \tilde{g}_{VV} \end{bmatrix} \odot \begin{bmatrix} 1 & \varepsilon_H^R \\ \varepsilon_V^R & 1 \end{bmatrix} \begin{bmatrix} 1 & \varepsilon_1^T \\ \varepsilon_2^T & 1 \end{bmatrix} \times \begin{bmatrix} S_{HH} & S_{HV} \\ S_{VH} & S_{VV} \end{bmatrix} \begin{bmatrix} 1 & \varepsilon_1^R \\ \varepsilon_2^R & 1 \end{bmatrix} \begin{bmatrix} 1 & \varepsilon_V^T \\ \varepsilon_H^T & 1 \end{bmatrix} \quad (11)$$

where $\varepsilon_1^T, \varepsilon_1^R, \varepsilon_2^T$, and ε_2^R are the crosstalk parameters of the RODAPARC. The 12 unknown distortion parameters of (4) need to be solved by means of 12 equations, which not only increase the complexity of the solution but also give rise to the loss of accuracy. The crosstalk parameters in (4) are merged as

$$\begin{bmatrix} M_{HH} & M_{HV} \\ M_{VH} & M_{VV} \end{bmatrix} = \begin{bmatrix} \tilde{g}_{HH} & \tilde{g}_{HV} \\ \tilde{g}_{VH} & \tilde{g}_{VV} \end{bmatrix} \odot \begin{bmatrix} 1+\varepsilon_H^R\varepsilon_2^T & \varepsilon_1^T+\varepsilon_H^R \\ \varepsilon_V^R+\varepsilon_2^T & \varepsilon_V^R\varepsilon_1^T+1 \end{bmatrix} \times \begin{bmatrix} S_{HH} & S_{HV} \\ S_{VH} & S_{VV} \end{bmatrix} \begin{bmatrix} 1+\varepsilon_1^R\varepsilon_H^T & \varepsilon_V^T+\varepsilon_1^R \\ \varepsilon_2^R+\varepsilon_H^T & \varepsilon_2^R\varepsilon_V^T+1 \end{bmatrix}. \quad (12)$$

Since the crosstalk parameters are quite small, terms of second order in (5) are negligible. Then, terms of first order are estimated as

$$\begin{bmatrix} M_{HH} & M_{HV} \\ M_{VH} & M_{VV} \end{bmatrix} = \begin{bmatrix} \tilde{g}_{HH} & \tilde{g}_{HV} \\ \tilde{g}_{VH} & \tilde{g}_{VV} \end{bmatrix} \odot \begin{bmatrix} 1 & a\varepsilon_H^R \\ b\varepsilon_V^R & 1 \end{bmatrix} \times \begin{bmatrix} S_{HH} & S_{HV} \\ S_{VH} & S_{VV} \end{bmatrix} \begin{bmatrix} 1 & d\varepsilon_V^T \\ c\varepsilon_H^T & 1 \end{bmatrix} \quad (13)$$

where a, b, c, and d denote the coefficients of the crosstalk parameters, respectively.

III. Theoretical PSM of the RODAPARC

The interaction between the incident electromagnetic wave and the target can be described by means of PSM. According to transceiver path of the RODAPARC, the theoretical PSM of the RODAPARC can be written as

$$\begin{bmatrix} S_{HH} & S_{HV} \\ S_{VH} & S_{VV} \end{bmatrix} = \sqrt{\frac{\sigma}{4\pi}} \begin{bmatrix} \frac{E_H^R}{P^T} \\ \frac{E_V^R}{P^T} \end{bmatrix} \begin{bmatrix} \frac{P^R}{E_H^T} & \frac{P^R}{E_V^T} \end{bmatrix} \quad (14)$$

where σ denotes the RCS of the RODAPARC at $\phi_r = 0°$ and $\phi_t = 0°$. ϕ_r and ϕ_t are the polarized rotation angles of the RODAPARC antennas, as shown in Fig. 1.

The near-field measurement mentioned in this article refers to the MIMO array using time-division multiplexing across transmit and receive elements through switch matrices [6], where the antenna array consists of 16 horn antenna elements

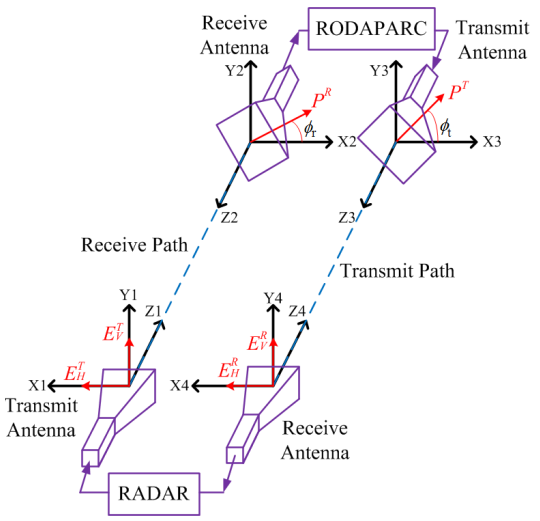

Fig. 1. Transceiver path of the RODAPARC with monostatic geometry.

and its length is 2 m. However, applying the far-field criterion [31] to the horn element with the size of 79 mm × 79 mm, the 5.4 m measurement distance is in the far field [32]. Therefore, the theoretical σ defined with the far-field hypothesis of the RODAPARC is given by [11]

$$\sigma = G_{loop}\frac{G_t G_r \lambda^2}{4\pi} \quad (15)$$

where G_t and G_r are the transmit and receive antenna gains, respectively; G_{loop} denotes the loop gain including amplifier gain, delay line, and other RF circuit losses. Considering the far-field hypothesis, we neglect the effect of the range on the RCS in receive and transmit paths.

In Fig. 1, the transceiver path includes two receive paths from the radar antenna transmitting horizontal (E_H^T)/vertical (E_V^T) polarization signal to the RODAPARC antenna receiving signal (P^R), and two transmit paths from the RODAPARC antenna transmitting signal (P^T) to the radar antenna receiving horizontal (E_H^R)/vertical (E_V^R) polarization signal.

A. Monostatic PSM

When the RODAPARC is applied in the monostatic case, we can express the transceiver path of the RODAPARC described by the following:

$$-E_H^T\cos\phi_r = P^R \quad (16a)$$
$$E_V^T\sin\phi_r = P^R \quad (16b)$$
$$-P^T\cos\phi_t = E_H^R \quad (16c)$$
$$P^T\sin\phi_t = E_V^R. \quad (16d)$$

According to (7) and (8), the PSM of the RODAPARC with monostatic geometry can be given by

$$S = \sqrt{\frac{\sigma}{4\pi}} \begin{bmatrix} \cos\phi_t\cos\phi_r & -\cos\phi_t\sin\phi_r \\ -\sin\phi_t\cos\phi_r & \sin\phi_t\sin\phi_r \end{bmatrix}. \quad (17)$$

B. Bistatic PSM

The RODAPARC using wide beam horn antennas is a good way to solve the calibration problem of the polarimetric MIMO array with different bistatic angles in the near-field measurement. To derive the bistatic PSM of the RODAPARC, the radiation electric field of antenna needs to be considered on the monostatic PSM. Since both the RODAPARC and the polarimetric MIMO array use horn antennas, the radiation electric field of the horn antenna can be simplified by Huygens' radiation electric field [33].

The radiation electric fields of the Huygens element on the x- and y-axes are expressed as follows:

$$\boldsymbol{p}_x = j\frac{E_0 s}{2\lambda r}e^{-jkr}(\boldsymbol{a}_\theta(\cos\theta+1)\cos\phi-\boldsymbol{a}_\phi(\cos\theta+1)\sin\phi) \tag{18a}$$

$$\boldsymbol{p}_y = j\frac{E_0 s}{2\lambda r}e^{-jkr}(\boldsymbol{a}_\theta(\cos\theta+1)\sin\phi+\boldsymbol{a}_\phi(\cos\theta+1)\cos\phi). \tag{18b}$$

The radiant electric field of the Huygens element with rotating angle ϕ_r can be written as

$$\boldsymbol{p}_{\phi_\mathrm{r}} = j\frac{E_0 s}{2\lambda r}e^{-jkr}\times(\boldsymbol{a}_\theta(\cos\theta+1)\cos(\phi-\phi_\mathrm{r}) -\boldsymbol{a}_\phi(\cos\theta+1)\sin(\phi-\phi_\mathrm{r})) \tag{18c}$$

where E_0 denotes the electric field on the Huygens element; s is the area of the Huygens element; λ is the wavelength; k is the wavenumber; and r, θ, and ϕ represent the radial distance, pitch angle, and azimuth angle in spherical coordinates, respectively. $\boldsymbol{a}_\theta$ and $\boldsymbol{a}_\phi$ are the pitch and azimuth unit vectors of radiation electric field, respectively.

In the horizontal plane ($\phi = 0$), the radiation electric field of the Huygens element on the x-axis is the E plate radiation electric field ($\boldsymbol{p}_x = \boldsymbol{p}^e$), and the radiation electric field of the Huygens element on the y-axis is the H plate radiation electric field ($\boldsymbol{p}_y = \boldsymbol{p}^h$). Equation (10) can be reduced to

$$\boldsymbol{p}_x = \boldsymbol{p}^e = j\frac{E_0 s}{2\lambda r}e^{-jkr}(\boldsymbol{a}_\theta(\cos\theta+1)) \tag{19a}$$

$$\boldsymbol{p}_y = \boldsymbol{p}^h = j\frac{E_0 s}{2\lambda r}e^{-jkr}(\boldsymbol{a}_\phi(\cos\theta+1)) \tag{19b}$$

$$\begin{aligned}\boldsymbol{p}_{\phi_\mathrm{r}} &= j\frac{E_0 s}{2\lambda r}e^{-jkr}(\boldsymbol{a}_\theta(\cos\theta+1)\cos(\phi_\mathrm{r}) +\boldsymbol{a}_\phi(\cos\theta+1)\sin(\phi_\mathrm{r}))\\ &= \boldsymbol{p}^e\cos(\phi_\mathrm{r})+\boldsymbol{p}^h\sin(\phi_\mathrm{r}).\end{aligned} \tag{19c}$$

It can be seen from (11c) that the radiation electric field of the Huygens element with any rotation angles can be synthesized by the E and H plate radiation electric fields in the horizontal plane. When the radiation electric field of the antenna is measured, the E and H plate radiation electric fields will be taken as its performance reference. Therefore, this result plays an invaluable role in the following derivation, which allows the horizontal ($\phi = 0$) radiation electric field of horn antenna with any rotation angles to be expressed through a known E and H plate radiation electric field.

Fig. 2 presents the transceiver path of the RODAPARC with bistatic geometry. In the horizontal plane (XOZ), Huygens' radiation electric field of the MIMO array and the

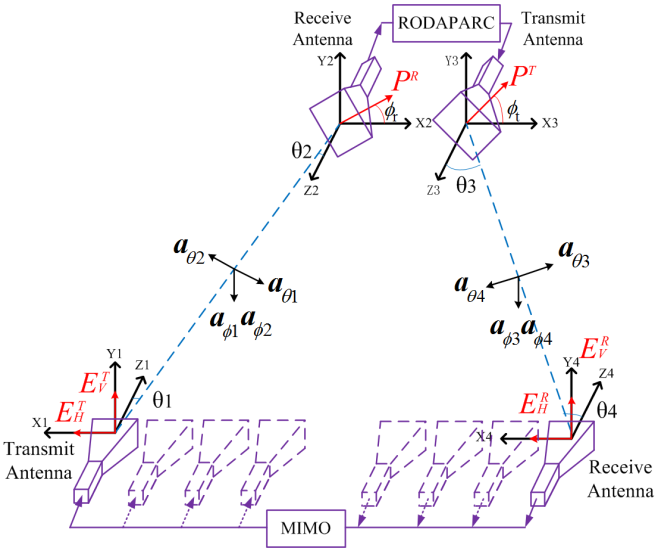

Fig. 2. Transceiver path of the RODAPARC with bistatic geometry.

RODAPARC can be given by

$$\boldsymbol{p}^{te}_{MIMO} = j\frac{E_0 s}{2\lambda r}e^{-jkr}(\boldsymbol{a}_{\theta_1}(\cos\theta_1+1)) \tag{20a}$$

$$\boldsymbol{p}^{th}_{MIMO} = j\frac{E_0 s}{2\lambda r}e^{-jkr}(\boldsymbol{a}_{\phi_1}(\cos\theta_1+1)) \tag{20b}$$

$$\boldsymbol{p}^{re}_{MIMO} = j\frac{E_0 s}{2\lambda r}e^{-jkr}(\boldsymbol{a}_{\theta_4}(\cos\theta_4+1)) \tag{20c}$$

$$\boldsymbol{p}^{rh}_{MIMO} = j\frac{E_0 s}{2\lambda r}e^{-jkr}(\boldsymbol{a}_{\phi_4}(\cos\theta_4+1)) \tag{20d}$$

$$\begin{aligned}\boldsymbol{p}^{r}_{PARC} &= j\frac{E_0 s}{2\lambda r}e^{-jkr}((\boldsymbol{a}_{\theta_2}(\cos\theta_2+1)\cos(\phi_\mathrm{r}) +\boldsymbol{a}_{\phi_2}(\cos\theta_2+1)\sin(\phi_\mathrm{r}))\\ &= \boldsymbol{p}^{re}_{PARC}\cos(\phi_\mathrm{r})+\boldsymbol{p}^{rh}_{PARC}\sin(\phi_\mathrm{r})\end{aligned} \tag{20e}$$

$$\begin{aligned}\boldsymbol{p}^{t}_{PARC} &= j\frac{E_0 s}{2\lambda r}e^{-jkr}(\boldsymbol{a}_{\theta_3}(\cos\theta_3+1)\cos(\phi_\mathrm{t}) +\boldsymbol{a}_{\phi_3}(\cos\theta_3+1)\sin(\phi_t))\\ &= \boldsymbol{p}^{te}_{PARC}\cos(\phi_t)+\boldsymbol{p}^{th}_{PARC}\sin(\phi_t)\end{aligned} \tag{20f}$$

where $\boldsymbol{p}^{te}_{MIMO}$, $\boldsymbol{p}^{th}_{MIMO}$, $\boldsymbol{p}^{re}_{MIMO}$, and $\boldsymbol{p}^{rh}_{MIMO}$ are E- and H-plane Huygens' radiation electric fields of the MIMO array, respectively. $\boldsymbol{p}^{te}_{PARC}$, $\boldsymbol{p}^{th}_{PARC}$, $\boldsymbol{p}^{re}_{PARC}$, and $\boldsymbol{p}^{rh}_{PARC}$ are E- and H-plane Huygens' radiation electric fields of the RODAPARC, respectively.

According to the relative position of the RODAPARC and the MIMO array, as shown in Fig. 2, the product of Huygens' radiation electric field on the transceiver path can be listed as

$$\boldsymbol{p}^{te}_{MIMO}\boldsymbol{p}^{r}_{PARC} \xrightarrow{\boldsymbol{a}_\theta\boldsymbol{a}_\phi=0} \boldsymbol{p}^{te}_{MIMO}(\boldsymbol{p}^{re}_{PARC}\cos\phi_\mathrm{r}) \xrightarrow[\boldsymbol{a}_{\phi_1}=\boldsymbol{a}_{\phi_2}=\boldsymbol{a}_{\phi_3}=\boldsymbol{a}_{\phi_4}]{\boldsymbol{a}_{\theta_1}=-\boldsymbol{a}_{\theta_2},\boldsymbol{a}_{\theta_3}=-\boldsymbol{a}_{\theta_4}} -p^{te}_{MIMO}(p^{re}_{PARC}\cos\phi_r) \tag{21a}$$

$$\boldsymbol{p}^{th}_{MIMO}\boldsymbol{p}^{r}_{PARC} \xrightarrow{\boldsymbol{a}_\theta\boldsymbol{a}_\phi=0} \boldsymbol{p}^{th}_{MIMO}(\boldsymbol{p}^{rh}_{PARC}\sin\phi_r) \xrightarrow[\boldsymbol{a}_{\phi_1}=\boldsymbol{a}_{\phi_2}=\boldsymbol{a}_{\phi_3}=\boldsymbol{a}_{\phi_4}]{\boldsymbol{a}_{\theta_1}=-\boldsymbol{a}_{\theta_2},\boldsymbol{a}_{\theta_3}=-\boldsymbol{a}_{\theta_4}} p^{th}_{MIMO}(p^{rh}_{PARC}\sin\phi_r) \tag{21b}$$

$$\boldsymbol{p}^{t}_{PARC}\boldsymbol{p}^{re}_{MIMO} \xrightarrow{\boldsymbol{a}_\theta\boldsymbol{a}_\phi=0} (\boldsymbol{p}^{te}_{PARC}\cos\phi_t)\boldsymbol{p}^{re}_{MIMO}$$

TABLE I
FOUR POLARIZATION COMBINATIONS OF THE RODAPARC

State	Rotation angle of receive antenna	Rotation angle of transmit antenna
1	0°	0°
2	0°	90°
3	90°	0°
4	90°	90°

$$\xrightarrow[\boldsymbol{a}_{\phi_1}=\boldsymbol{a}_{\phi_2}=\boldsymbol{a}_{\phi_3}=\boldsymbol{a}_{\phi_4}]{\boldsymbol{a}_{\theta_1}=-\boldsymbol{a}_{\theta_2},\boldsymbol{a}_{\theta_3}=-\boldsymbol{a}_{\theta_4}} -(p^{te}_{PARC}\cos\phi_t)p^{re}_{MIMO} \tag{21c}$$

$$\boldsymbol{p}^{t}_{PARC}\boldsymbol{p}^{rh}_{MIMO} \xrightarrow{\boldsymbol{a}_\theta\boldsymbol{a}_\phi=0} (\boldsymbol{p}^{th}_{PARC}\sin\phi_t)\boldsymbol{p}^{rh}_{MIMO} \xrightarrow[\boldsymbol{a}_{\phi_1}=\boldsymbol{a}_{\phi_2}=\boldsymbol{a}_{\phi_3}=\boldsymbol{a}_{\phi_4}]{\boldsymbol{a}_{\theta_1}=-\boldsymbol{a}_{\theta_2},\boldsymbol{a}_{\theta_3}=-\boldsymbol{a}_{\theta_4}} (p^{th}_{PARC}\sin\phi_t)p^{rh}_{MIMO}. \tag{21d}$$

The radiation electric field pattern of horn antennas can be obtained by integrating Huygens' radiation electric field on the aperture of horn antenna. Therefore, the transceiver path can be completely expressed by the radiation electric field pattern of horn antennas as follows:

$$-E^T_H P^{TE}_{MIMO}(P^{RE}_{PARC}\cos\phi_r) = P^R \tag{22a}$$

$$E^T_V P^{TH}_{MIMO}(P^{RH}_{PARC}\sin\phi_r) = P^R \tag{22b}$$

$$-P^T P^{RE}_{MIMO}(P^{TE}_{PARC}\cos\phi_t) = E^R_H \tag{22c}$$

$$P^T P^{RH}_{MIMO}(P^{TH}_{PARC}\sin\phi_t) = E^R_V \tag{22d}$$

where P^{TE}_{MIMO}, P^{TH}_{MIMO}, P^{RE}_{MIMO}, and P^{RH}_{MIMO} are the E- and H-plane radiation electric field patterns of the MIMO array, respectively. P^{TE}_{PARC}, P^{TH}_{PARC}, P^{RE}_{PARC}, and P^{RH}_{PARC} are the E- and H-plane radiation electric field patterns of the RODAPARC, respectively. Therefore, from (14), we have the bistatic PSM of RODAPARC (23), shown at the bottom of this page.

IV. POLARIMETRIC CALIBRATION PROCEDURE

The procedure consists of two steps.

Step 1: The RODAPARC should be mounted in the working area, where all transceiver channels of the polarimetric MIMO array are measured in time-division mode. For each transceiver channel, we can obtain the E- and H-plane radiation electric field patterns of (15) according to relative position of the array and the RODAPARC. The return signals can be received by controlling the different polarization combinations of the RODAPARC antennas to solve all distortion parameters.

Step 2: The polarimetric MIMO array measures a passive polarimetric calibrator. The return signals are calibrated using distortion parameters solved by Step 1; then, the calibrated signals continue to be optimized by four coefficients.

In this article, we use the four polarization combinations of the RODAPARC listed in Table I. Substituting (15) into (6), we have

$$\begin{bmatrix} M^1_{HH} & M^1_{HV} \\ M^1_{VH} & M^1_{VV} \end{bmatrix} = \sqrt{\frac{\sigma}{4\pi}} P^{TE}_{PARC} P^{RE}_{MIMO} P^{TE}_{MIMO} P^{RE}_{PARC} \times \begin{bmatrix} \tilde{g}_{HH} & \tilde{g}_{HV} d\varepsilon^T_V \\ \tilde{g}_{VH} b\varepsilon^R_V & \tilde{g}_{VV} b\varepsilon^R_V d\varepsilon^T_V \end{bmatrix} \tag{24a}$$

$$\begin{bmatrix} M^2_{HH} & M^2_{HV} \\ M^2_{VH} & M^2_{VV} \end{bmatrix} = \sqrt{\frac{\sigma}{4\pi}} P^{TE}_{PARC} P^{RE}_{MIMO} P^{TH}_{MIMO} P^{RH}_{PARC} \times \begin{bmatrix} -\tilde{g}_{HH} c\varepsilon^T_H & -\tilde{g}_{HV} \\ -\tilde{g}_{VH} c\varepsilon^R_V b\varepsilon^T_H & -\tilde{g}_{VV} b\varepsilon^R_V \end{bmatrix} \tag{24b}$$

$$\begin{bmatrix} M^3_{HH} & M^3_{HV} \\ M^3_{VH} & M^3_{VV} \end{bmatrix} = \sqrt{\frac{\sigma}{4\pi}} P^{TH}_{PARC} P^{RH}_{MIMO} P^{TE}_{MIMO} P^{RE}_{PARC} \times \begin{bmatrix} -\tilde{g}_{HH} a\varepsilon^R_H & -\tilde{g}_{HV} a\varepsilon^R_H d\varepsilon^T_V \\ -\tilde{g}_{VH} & -\tilde{g}_{VV} d\varepsilon^T_V \end{bmatrix} \tag{24c}$$

$$\begin{bmatrix} M^4_{HH} & M^4_{HV} \\ M^4_{VH} & M^4_{VV} \end{bmatrix} = \sqrt{\frac{\sigma}{4\pi}} P^{TH}_{PARC} P^{RH}_{MIMO} P^{TH}_{MIMO} P^{RH}_{PARC} \times \begin{bmatrix} \tilde{g}_{HH} a\varepsilon^R_H c\varepsilon^T_H & \tilde{g}_{HV} a\varepsilon^R_H \\ \tilde{g}_{VH} c\varepsilon^T_H & \tilde{g}_{VV} \end{bmatrix}. \tag{24d}$$

The four polarization channel gain parameters can be obtained from the return signals compensated by the antenna patterns, which may be expressed as

$$\tilde{g}_{HH} = \sqrt{\frac{4\pi}{\sigma}} \frac{M^1_{HH}}{P^{RE}_{PARC} P^{TE}_{PARC} P^{RE}_{MIMO} P^{TE}_{MIMO}} \tag{25a}$$

$$\tilde{g}_{HV} = -\sqrt{\frac{4\pi}{\sigma}} \frac{M^2_{HV}}{P^{RE}_{PARC} P^{TH}_{PARC} P^{RE}_{MIMO} P^{TH}_{MIMO}} \tag{25b}$$

$$\tilde{g}_{VH} = -\sqrt{\frac{4\pi}{\sigma}} \frac{M^3_{VH}}{P^{RH}_{PARC} P^{TE}_{PARC} P^{RH}_{MIMO} P^{TE}_{MIMO}} \tag{25c}$$

$$\tilde{g}_{VV} = \sqrt{\frac{4\pi}{\sigma}} \frac{M^4_{VV}}{P^{RH}_{PARC} P^{TH}_{PARC} P^{RH}_{MIMO} P^{TH}_{MIMO}}. \tag{25d}$$

The four crosstalk parameters can be given by

$$a\varepsilon^R_H = -\frac{M^4_{HV} P^{TE}_{PARC} P^{RE}_{MIMO}}{M^2_{HV} P^{TH}_{PARC} P^{RH}_{MIMO}} \tag{26a}$$

$$b\varepsilon^R_V = -\frac{M^1_{VH} P^{TH}_{PARC} P^{RH}_{MIMO}}{M^3_{VH} P^{TE}_{PARC} P^{RE}_{MIMO}} \tag{26b}$$

$$c\varepsilon^T_H = -\frac{M^2_{HH} P^{TE}_{MIMO} P^{RE}_{PARC}}{M^1_{HH} P^{TH}_{MIMO} P^{RH}_{PARC}} \tag{26c}$$

$$d\varepsilon^T_V = -\frac{M^1_{HV} P^{TH}_{MIMO} P^{RH}_{PARC}}{M^2_{HV} P^{TE}_{MIMO} P^{RE}_{PARC}}. \tag{26d}$$

The four unknown coefficients (a, b, c, and d) are finely turned and determined through a passive polarimetric calibrator with large RCS and bistatic insensitivity, which makes the calibrated PSM closer to its truth. Here, we take a perfect

$$\mathbf{S} = \sqrt{\frac{\sigma}{4\pi}} \begin{bmatrix} \cos\phi_t \cos\phi_r P^{TE}_{PARC} P^{RE}_{MIMO} P^{TE}_{MIMO} P^{RE}_{PARC} & -\cos\phi_t \sin\phi_r P^{TE}_{PARC} P^{RE}_{MIMO} P^{TH}_{MIMO} P^{RH}_{PARC} \\ -\sin\phi_t \cos\phi_r P^{TH}_{PARC} P^{RH}_{MIMO} P^{TE}_{MIMO} P^{RE}_{PARC} & \sin\phi_t \sin\phi_r P^{TH}_{PARC} P^{RH}_{MIMO} P^{TH}_{MIMO} P^{RH}_{PARC} \end{bmatrix} \tag{23}$$

.

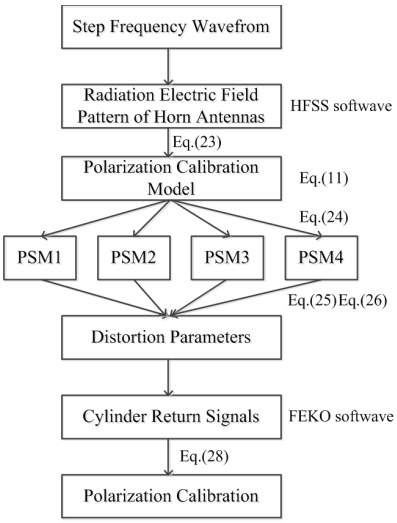

Fig. 3. Flowchart for simulation.

electric conductor (PEC) cylinder as the passive polarimetric calibrator with a height of 107 mm and a radius of 115 mm. Based on the theoretical PSM of the cylinder, the normalized cross-polarization signals calibrated using the distortion parameters should be zero

$$S_{HV}/S_{HH} = 0$$
$$S_{VH}/S_{HH} = 0. \tag{27}$$

There are no analytic solutions to these four coefficients. Mathematical optimization is applied to obtain a numerical solution given as

$$\mathbf{X} = \arg\min\left(\left|\frac{S_{VH}(a,b,c,d)}{S_{HH}}\right| + \left|\frac{S_{HV}(a,b,c,d)}{S_{HH}}\right|\right)$$
$$\text{s.t.} \left|\left|\frac{S_{VH}(a,b,c,d)}{S_{HH}}\right|(\text{dB})\right.$$
$$\left. - \left|\frac{S_{HV}(a,b,c,d)}{S_{HH}}\right|(\text{dB})\right| \le \eta(\text{dB}) \tag{28}$$

where $\mathbf{X} = [a,\ b,\ c,\ d]$, η is a threshold that prevents the calibrated signals from mutating. The range of these four coefficients can be estimated by the known cross-polarization level of the antenna in the RODAPARC and the MIMO array. In this range, these four coefficients are finely turned to obtain the crosstalk parameters close to the true value according to (20).

A hybrid simulation of one transceiver channel with 10° bistatic angle is conducted to validate the polarimetric calibration procedure, and the flowchart is shown in Fig. 3. First of all, we simulate the PSM of the RODAPARC using step frequency waveform (8–12 GHz) and the E-/H-plane radiation electric field patterns of horn antenna obtained by *HFSS* software [34]. Considering the crosstalk of the RODAPARC, return signals of the transceiver channel can be represented as (11) with 12 distortion parameters ($\tilde{g}_{HH} = 1.2$ dB, $\tilde{g}_{HV} = 0.3$ dB, $\tilde{g}_{VH} = 1$ dB, $\tilde{g}_{VV} = 0.2$ dB, $\varepsilon_H^R = -39$ dB, $\varepsilon_V^R = -33$ dB, $\varepsilon_H^T = -41$ dB, $\varepsilon_V^T = -34$ dB, and $\varepsilon_1^T = \varepsilon_1^R = \varepsilon_2^T = \varepsilon_2^R = -40$ dB). Then, in order

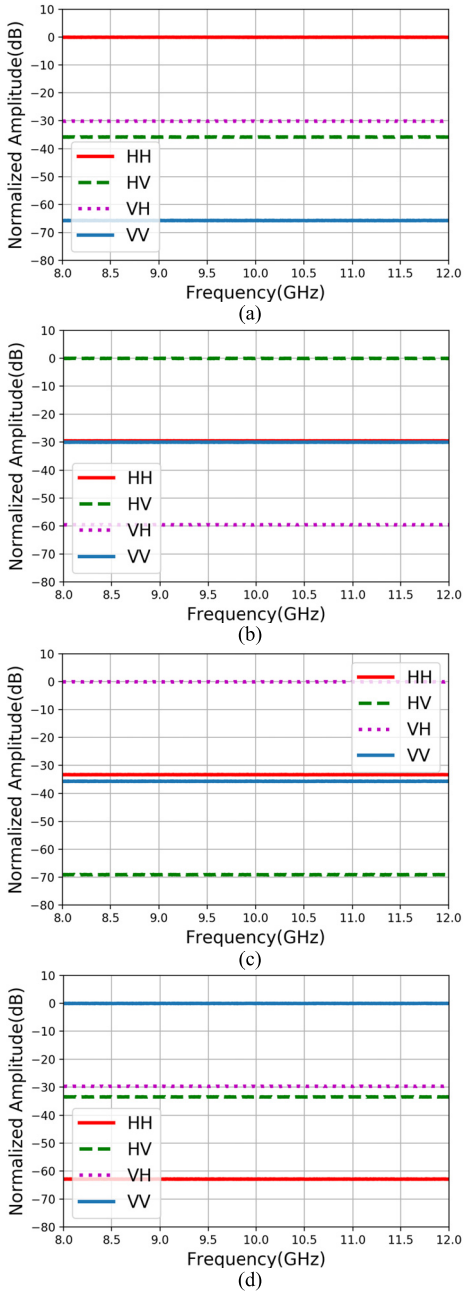

Fig. 4. Four PSMs of RODAPARC given in Table I. (a) State1. (b) State2. (c) State3. (d) State4.

to calibrate the transceiver channel, we need to obtain four PSMs of the RODAPARC, as shown in Fig. 4. According to the four PSMs, the eight distortion parameters can be solved using (25) and (26).

Finally, the four polarization return signals of a cylinder are simulated to illustrate how to detect the mutation using *FEKO* software [35]. The raw return signals are contaminated by (10) to generate uncalibrated return signals, as shown in Fig. 5(a). The signals are calibrated through the eight distortion parameters. As can be seen from Fig. 5(b), after calibration, the average levels of the two cross-polarized signals reach about −60 dB. However, the difference between the two cross-polarized signals is particularly large at 9.2 and 10.6 GHz,

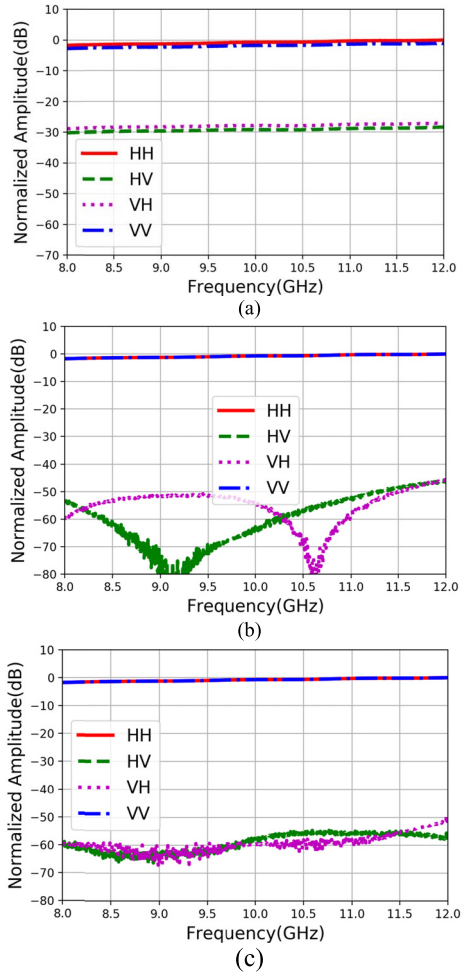

Fig. 5. Simulation result of polarimetric calibration. (a) Uncalibrated return signals, calibrated return signals (b) with mutation, and (c) without mutation.

Fig. 6. Photograph of the RODAPARC.

which is inconsistent with the truth. In order to prevent the mutation of calibration results, it is necessary to put additional constraint on the optimization. To do so, the threshold η is set to 10 dB. When the difference is less than 10 dB, we believe that the estimated crosstalk parameters are close to the true values, as shown in Fig. 5(c).

V. Experimental Results

A. Calibration System of the Polarimetric MIMO Array

Fig. 6 shows the RODAPARC that is composed of two horn antennas, two motors, and microwave circuits [29]. The

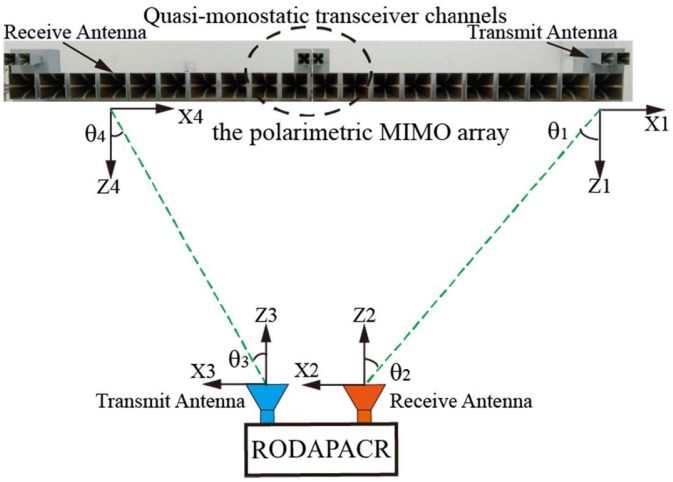

Fig. 7. Configuration of the polarimetric MIMO array calibrated by the RODAPARC.

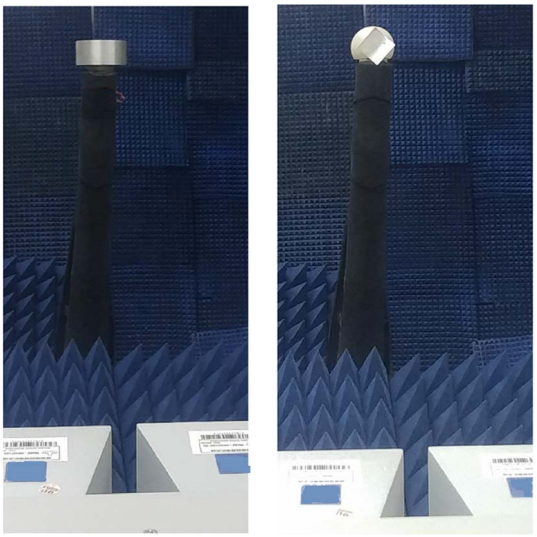

Fig. 8. Measurements on (a) small cylinder and (b) dihedral reflector.

receive and transmit antennas can independently rotate around the radar line of sight to any angle by controlling the motor with encoder. The unique features for the RODAPARC include that various forms of PSM can be obtained through a flexible combination of the rotation and initial polarization of the two antennas, and the adjustable RCS makes the return signals have high SNR.

An experimental polarimetric MIMO array at X-band has been upgraded based on the radar system in [6]. It can be seen from Fig. 7 that the polarimetric MIMO array consists of 20 receive elements and 6 transmit elements, where the combinations among them synthesize 80 transceiver channels. The calibration of the polarimetric MIMO array is implemented using the RODAPARC and a big metal cylinder. A small PEC cylinder with a height of 89 mm and a radius of 95 mm and a PEC rectangular dihedral reflector with a size of 90 mm $\times$ 90 mm are used as classic targets to evaluate the performance of the calibration, as shown in Fig. 8.

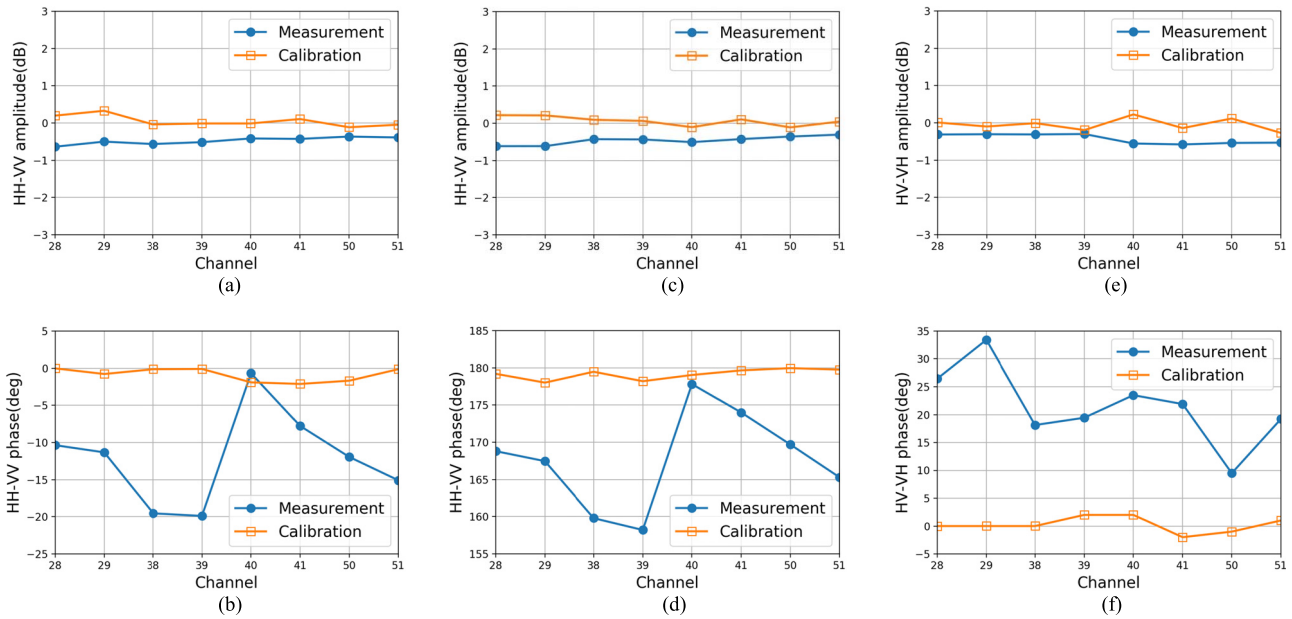

Fig. 9. Polarization channel gain error in quasi-monostatic transceiver channels. (a) Amplitude and (b) phase for small cylinder. (c) Amplitude and (d) phase for 0° rotated dihedral reflector. (e) Amplitude and (f) phase for 45° rotated dihedral reflector.

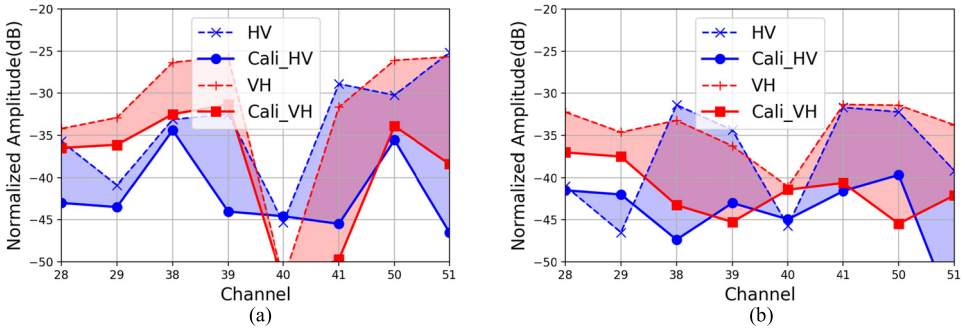

Fig. 10. Cross-polarization levels of (a) small cylinder and (b) 0° rotated dihedral reflector in quasi-monostatic transceiver channels.

TABLE II
MEASUREMENT PARAMETERS

Parameters	Values
Radar frequency(GHz)	8.0-12.0
Frequency sampling points	801
Measurement distance(m)	5.4
Channel number	80
Range of the quasi-monostatic angles	<2°
Range of the bistatic angles	2°~10.5°

The RCS level of the dihedral reflector is higher than that of the two cylinders. Because the scattering of the dihedral reflector is sensitive to bistatic angles, the 80 transceiver channels are divided into two groups: one consists of eight transceiver channels formed by two transmit elements and four receive elements located at the array center, which is called as the quasi-monostatic transceiver channel, and the left is called as the bistatic transceiver channel. The space between two receive elements is 90 mm in the polarimetric MIMO array. The bistatic angles of eight quasi-monostatic transceiver channels are less than 3°. The measurement parameters are listed in Table II. In Sections V-B and V-C, we will present and discuss the calibration results from these two groups.

B. Quasi-Monostatic Case

Using the distortion parameters derived from the procedure previously described, we reprocess the return signals of the cylinder and dihedral reflector to verify the calibration results. The PSMs of the small cylinder and the θ° rotated dihedral reflector are given by

$$\mathbf{S}^{c} = \begin{bmatrix} -1 & 0 \\ 0 & -1 \end{bmatrix} \tag{29a}$$

$$\mathbf{S}^{D\theta} = \begin{bmatrix} -\cos 2\theta & \sin 2\theta \\ \sin 2\theta & \cos 2\theta \end{bmatrix}. \tag{29b}$$

Therefore, the PSMs of the small cylinder and the 0° and 45° rotated dihedral reflector are substituted into polarimetric signal model (3), as follows:

$$\begin{cases} M^{C}_{HH} = -\tilde{g}_{HH} \\ M^{C}_{HV} = \tilde{g}_{HV}\left(-\varepsilon^{T}_{V} - \varepsilon^{R}_{H}\right) \\ M^{C}_{VH} = \tilde{g}_{VH}\left(-\varepsilon^{R}_{V} - \varepsilon^{T}_{H}\right) \\ M^{C}_{VV} = -\tilde{g}_{VV} \end{cases} \tag{30a}$$

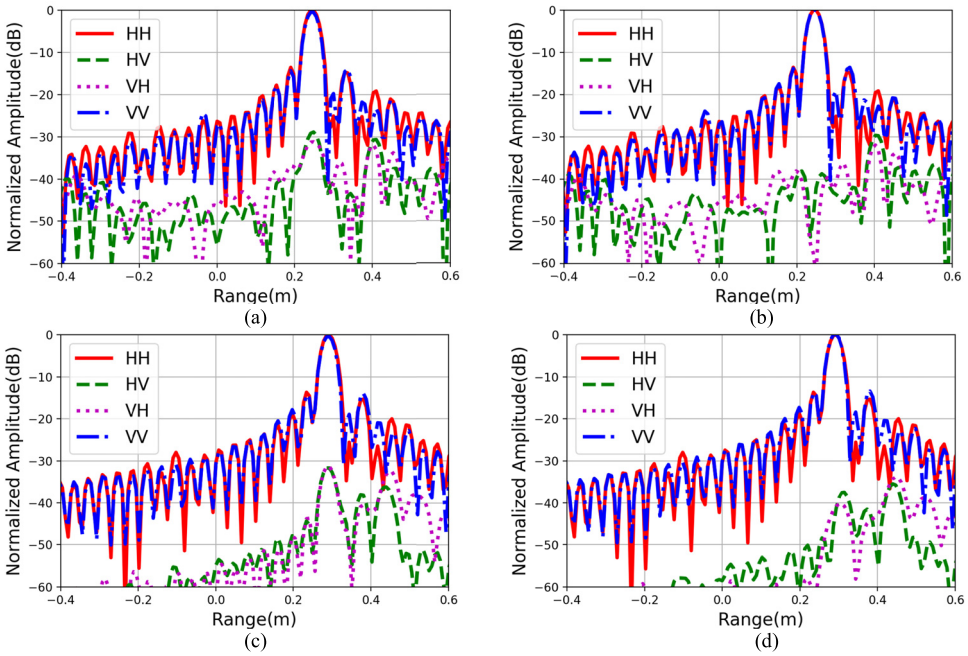

Fig. 11. HRRPs of (a) uncalibrated, (b) calibrated small cylinder, (c) uncalibrated, and (d) calibrated 0° rotated dihedral reflector in Fig. 12 polarization signatures for the small cylinder in the transceiver channel 41.

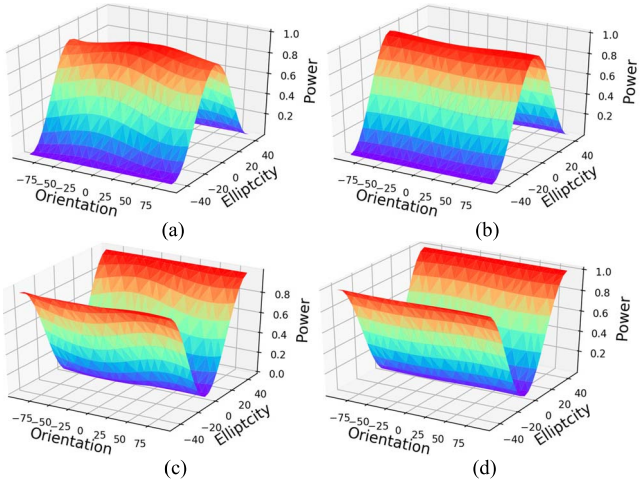

Fig. 12. Polarization signatures for the 0° rotated dihedral in the transceiver channel 41. (a) Uncalibrated and (b) calibrated copolar signature. (c) Uncalibrated and (d) calibrated cross-polar signature. The power of each response is normalized to the corresponding maximum.

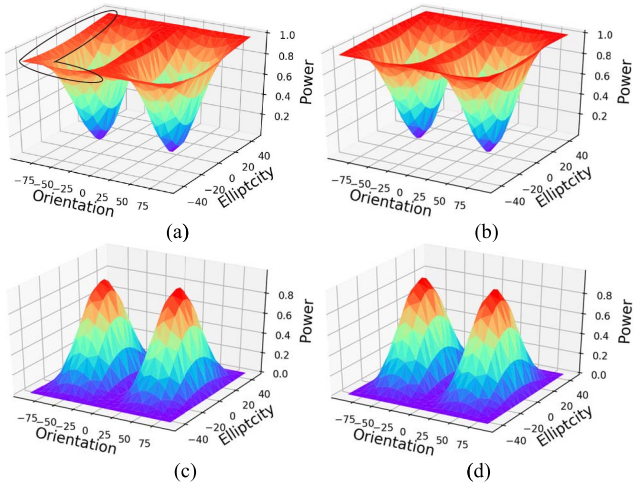

Fig. 13. Polarization signatures for the small cylinder in the transceiver channel 41. (a) uncalibrated and (b) calibrated copolar signature; (c) uncalibrated and (d) calibrated cross-polar signature. The power of each response is normalized to the corresponding maximum.

$$\begin{cases} M_{HH}^{D0} = -\tilde{g}_{HH} \\ M_{HV}^{D0} = \tilde{g}_{HV}\left(-\varepsilon_V^T + \varepsilon_H^R\right) \\ M_{VH}^{D0} = \tilde{g}_{VH}\left(-\varepsilon_V^R + \varepsilon_H^T\right) \\ M_{VV}^{D0} = \tilde{g}_{VV} \end{cases} \tag{30b}$$

$$\begin{cases} M_{HH}^{D45} = \tilde{g}_{HH}\left(\varepsilon_H^T + \varepsilon_H^R\right) \\ M_{HV}^{D45} = \tilde{g}_{HV} \\ M_{VH}^{D45} = \tilde{g}_{VH} \\ M_{VV}^{D45} = \tilde{g}_{VV}\left(\varepsilon_V^T + \varepsilon_V^R\right). \end{cases} \tag{30c}$$

Through the above equations, we observe that the calibration performance can be evaluated by the three objects, where the four crosstalk parameters can be verified by the small cylinder and the 0° rotated dihedral reflector, while the co-polarization level of 45° rotated dihedral is ignored because of the difficulty of rotating the dihedral reflector to 45° accurately. The small signals (M_{HH}^{D45} and M_{VV}^{D45}) are much more susceptible to the rotation angle of the dihedral reflector than the big signals (M_{HV}^{D45} and M_{VH}^{D45}).

Fig. 9 shows typical plots of polarization channel gain error for the small cylinder and the 0° and 45° rotated dihedral reflector in quasi-monostatic transceiver channels, where the x-coordinate represents the quasi-monostatic transceiver channel number.

The polarization channel gain error represents HH-VV polarization level (HH divided by VV) of the small cylinder

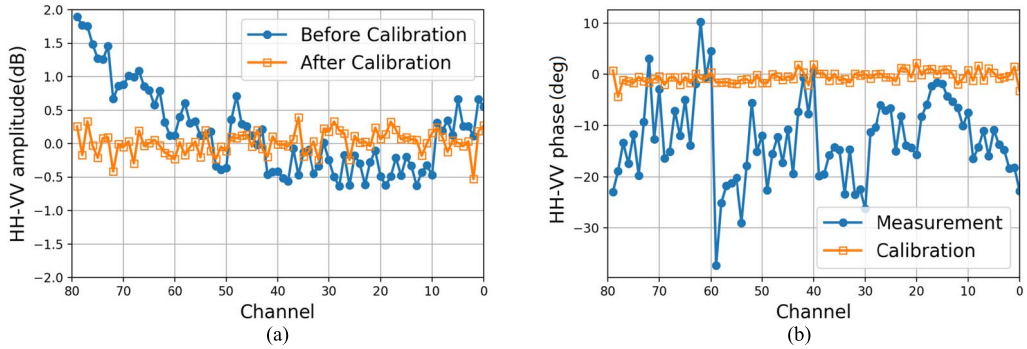

Fig. 14. (a) Amplitude and (b) phase of polarization channel gain error for the small cylinder in all transceiver channels.

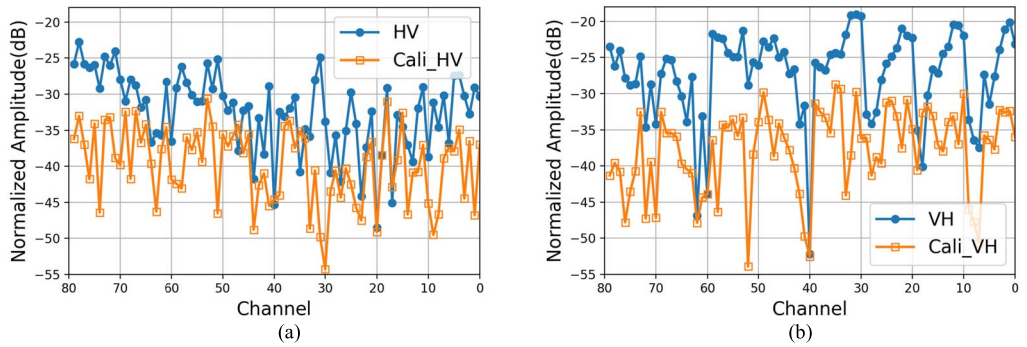

Fig. 15. (a) HV and (b) VH polarization levels of the small cylinder in all transceiver channels.

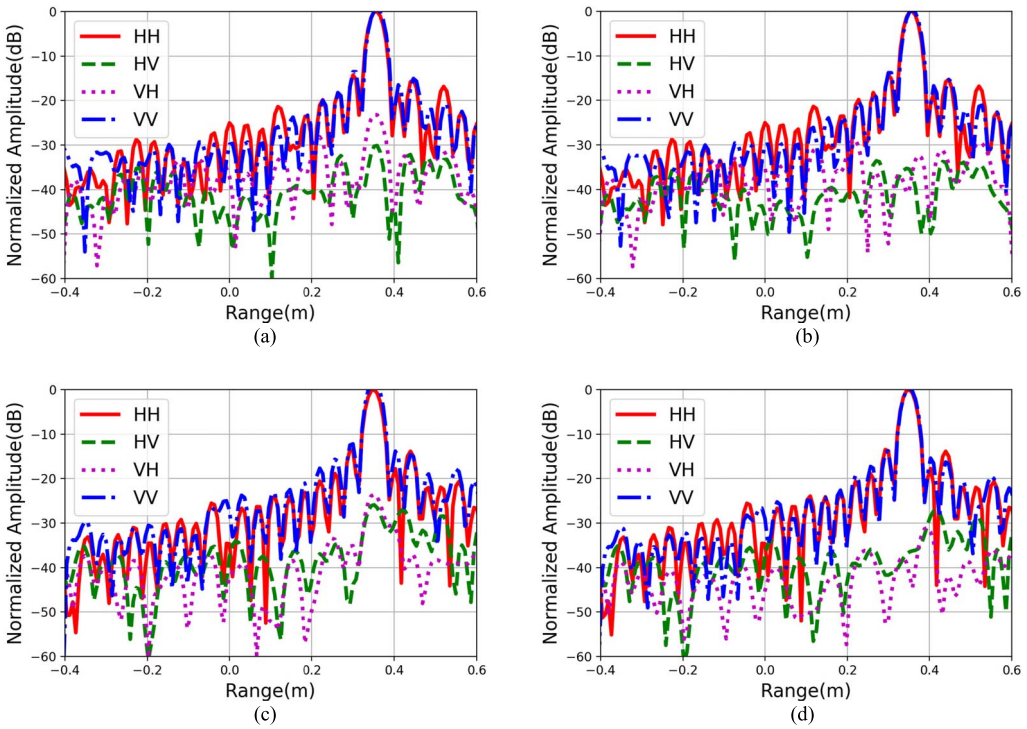

Fig. 16. HRRP of the small cylinder in (a) uncalibrated and (b) calibrated transceiver channel 0. (c) Uncalibrated and (d) calibrated transceiver channel 79.

and the 0° rotated dihedral reflector, and HV-VH polarization level (HV divided by VH) of 45° rotated dihedral reflector. After calibration, the error is decreased obviously. The calibration results are identical to the theoretical analysis.

Calibrated and uncalibrated cross-polarization levels of the small cylinder and the 0° rotated dihedral reflector in quasi-monostatic transceiver channels are plotted in Fig. 10. Distinct performances of the antenna elements in the polarimetric

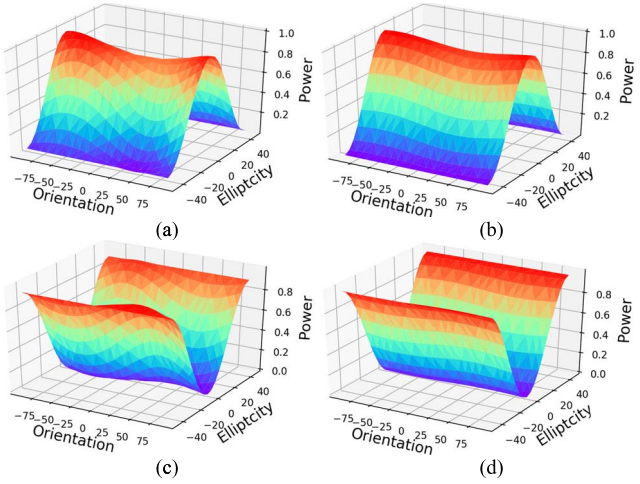

Fig. 17. Polarization signatures for the small cylinder in the transceiver channel 0. (a) Uncalibrated and (b) calibrated copolar signature. (c) Uncalibrated and (d) calibrated cross-polar signature. The power of each response is normalized to the corresponding maximum.

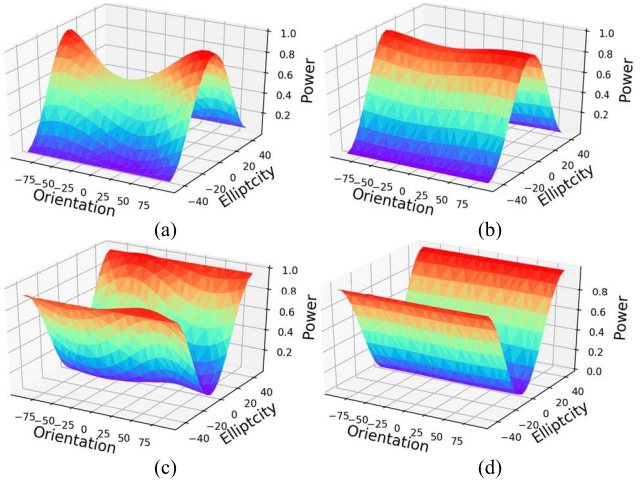

Fig. 18. Polarization signatures for the small cylinder in the transceiver channel 79. (a) Uncalibrated and (b) calibrated copolar signature. (c) Uncalibrated and (d) calibrated cross-polar signature. The power of each response is normalized to the corresponding maximum.

MIMO array make the cross-polarization level of each transceiver channel different. Due to the limitation of measurement environment, when the cross-polarization level of transceiver channel is below −40 dB, it is difficult to be calibrated to a lower level. It is worth noting that the cross-polarization level of the transceiver channel 40 reaches −40 dB. Therefore, we ignore the crosstalk parameters and only use polarization channel gain parameters to calibrate the transceiver channel 40. If the cross-polarization level of the transceiver channel is much higher than −35 dB, it can usually be calibrated to be below −35 dB, as shown in Fig. 10. It is also seen that the calibration results (VH: −40.5 dB and HV: −41.2 dB) of the dihedral reflector with higher signal-to-clutter ratio are better than that (VH: −37.3 dB and HV: −39.9 dB) of the small cylinder.

Fig. 11 shows the high-resolution range profiles (HRRPs) [36] of the cylinder and the 0° rotated dihedral reflector before and after the calibration in the transceiver channel 41. It can be seen from the results that the cross-polarization level is reduced by approximately 20 dB after calibration.

The polarization signatures for the small cylinder and the 0° rotated dihedral reflector in the transceiver channel 41 are, respectively, given in Figs. 12 and 13. After calibration, the polarization signatures are similar to the ideal polarization signatures for the small cylinder. Before calibration, the return signals of the 0° rotated dihedral reflector have high polarimetric isolation up to 32 dB [see Fig. 11(c)], which makes uncalibrated and calibrated polarization signatures almost the same, as shown in Fig. 13.

C. Bistatic Case

The proposed polarimetric calibration has been validated for the quasi-monostatic transceiver channels in Section V-B. We adopt it to calibrate all transceiver channels with relatively large bistatic angles. The dihedral reflector whose scattering is

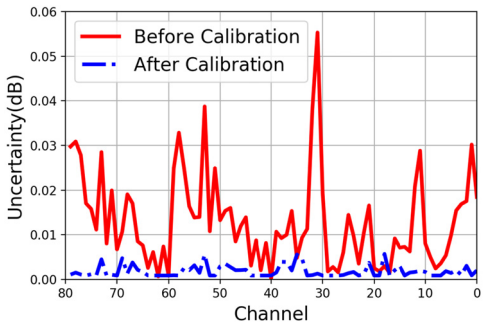

Fig. 19. Uncertainty caused by cross-polarization.

sensitive to bistatic angles will not be utilized in this section. The polarization channel gain error for the small cylinder in all transceiver channels is shown in Fig. 14. Before calibration, the transceiver channels 70–80 have HH-VV amplitude in excess of 1 dB due to the antenna performance or array installation. HH-VV amplitude of other transceiver channels varies from −1 to 1 dB. Furthermore, maximal HH-VV phase is up to −35° in the transceiver channel 59.

After calibration, the HH-VV has an upper limit of ±0.5 dB in amplitude and ±3° in phase. Fig. 15 shows the calibrated and uncalibrated cross-polarization level of the small cylinder in all transceiver channels. The VH polarization levels of all transceiver channels are higher than the HV polarization levels, and the average VH and HV polarization levels are −27.2 and −32.2 dB, respectively. The VH and HV polarization levels are lowered to −36.9 and −38.7 dB after calibration, respectively.

For examples, we consider the transceiver channels 0 and 79, as shown in Fig. 16. It can be seen from the normalized HRRP of the small cylinder that the HV and VH polarization levels (−30.2 and −23.1 dB) of the channel 0 are calibrated to −37.1 and −36.5 dB, while the HV and VH polarization levels (−25.8 and −23.4 dB) of the channel 79 are calibrated to −36.6 and −39.8 dB. In Figs. 17 and 18, we plot polarization signatures for the small cylinder in the two

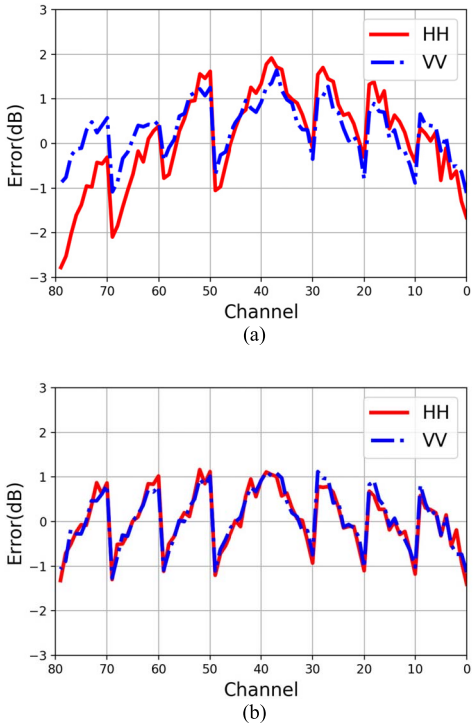

Fig. 20. Discrepancies between the measured and computed RCS of the small cylinder: (a) before and (b) after calibration for HH and VV polarizations.

transceiver channels. The calibrated polarization signatures after calibration have been significantly improved.

In RCS measurements, there are many uncertainty sources, where some of the most important sources are assigned hypothetical values, and the less important entries are assigned 0 dB [37]. The main interest of the measurement of the small cylinder is to identify the uncertainty sources like positioning defects of the cylinder on its support, the measurement stability, and cross-polarization. To simply the uncertainty analysis, we only consider the uncertainty caused by cross-polarization, as shown in Fig. 19. It can be found that the uncertainty decreases significantly after calibration. In addition, we show the discrepancy between measured and computed RCS of the small cylinder for two co-polarizations in Fig. 20. As expected, the discrepancies after calibration are smaller than before calibration. In Fig. 20(b), the error changes regularly with the channel number due to the antenna pattern, which can be compensated in [6].

VI. Conclusion

Calibration of a polarimetric MIMO array with horn elements for near-field measurement has been investigated in this article. A RODAPARC whose wide antenna beam can cover the whole array as well as a metal cylinder are used as the calibrators. The theoretical PSM of the RODAPARC with different antenna rotation angles is derived from Huygens' radiation electric field, which is applicable to different bistatic angles. A polarimetric signal model which merges the RODAPARC's own crosstalk is developed such that the true crosstalk of the array may be obtained through the measurement of two calibrators.

Experiments are conducted on a polarimetric MIMO array with 80 transceiver channels and result in excellent calibration performance. It is seen that the polarization isolation improvement is about 16 dB, and the polarization channel gain error is reduced to be within ± 0.5 dB in amplitude and $\pm 3^\circ$ in phase. The calibrated polarization signatures for classic objects are highly consistent with the theoretical results.

References

[1] D. W. Bliss, K. W. Forsythe, A. O. Hero, and A. F. Yegulalp, "Environmental issues for MIMO capacity," *IEEE Trans. Signal Process.*, vol. 50, no. 9, pp. 2128–2142, Sep. 2002.

[2] E. Fishler, A. Haimovich, R. Blum, D. Chizhik, L. Cimini, and R. Valenzuela, "MIMO radar: An idea whose time has come," in *Proc. the IEEE Radar Conf.*, Apr. 2004, pp. 71–78.

[3] J. Li and P. Stoica, "MIMO radar with collocated antennas," *IEEE Signal Process. Mag.*, vol. 24, no. 5, pp. 106–114, Oct. 2007.

[4] A. Haimovich, R. Blum, and L. Cimini, "MIMO radar with widely separated antennas," *IEEE Signal Process. Mag.*, vol. 25, no. 1, pp. 116–129, Dec. 2008.

[5] T. Zeng, C. Mao, C. Hu, X. Yang, and W. Tian, "Multi-static MIMO-SAR three dimensional deformation measurement system," in *Proc. IEEE 5th Asia–Pacific Conf. Synth. Aperture Radar (APSAR)*, Singapore, Sep. 2015, pp. 297–301.

[6] Y. Liu, X. Xu, and G. Xu, "MIMO radar calibration and imagery for near-field scattering diagnosis," *IEEE Trans. Aerosp. Electron. Syst.*, vol. 54, no. 1, pp. 442–452, Feb. 2018.

[7] M. W. Whitt, F. T. Ulaby, P. Polatin, and V. V. Liepa, "A general polarimetric radar calibration technique," *IEEE Trans. Antennas Propag.*, vol. 39, no. 1, pp. 62–67, Jan. 1991.

[8] T.-J. Chen, T.-H. Chu, and F.-C. Chen, "A new calibration algorithm of wide-band polarimetric measurement system," *IEEE Trans. Antennas Propag.*, vol. 39, no. 8, pp. 1188–1192, Aug. 1991.

[9] W. Wiesbeck and S. Riegger, "A complete error model for free space polarimetric measurements," *IEEE Trans. Antennas Propag.*, vol. 39, no. 8, pp. 1105–1111, Aug. 1991.

[10] A. Freeman, Y. Shen, and C. L. Werner, "Polarimetric SAR calibration experiment using active radar calibrators," *IEEE Trans. Geosci. Remote Sens.*, vol. 28, no. 2, pp. 224–240, Mar. 1990.

[11] K. Sarabandi, Y. Oh, and F. T. Ulaby, "Performance characterization of polarimetric active radar calibrators and a new single antenna design," *IEEE Trans. Antennas Propag.*, vol. 40, no. 10, pp. 1147–1154, Oct. 1992.

[12] J. J. Ahne, K. Sarabandi, and F. T. Ulaby, "Design and implementation of single antenna polarimetric active radar calibrators," in *Proc. IEEE Antennas Propag. Soc. Int. Symp.*, Jul. 1993, pp. 1280–1283.

[13] M. Jirousek, B. J. Döring, D. Rudolf, S. Raab, and M. Schwerdt, "Development of the highly accurate DLR Kalibri transponder," in *Proc. Eur. Conf. Synth. Aperture Radar*, Berlin, Germany, 2014, pp. 1–4.

[14] D. Rudolf, S. Raab, B. J. Döring, M. Jirousek, J. Reimann, and M. Schwerdt, "Absolute radiometric calibration of the novel DLR 'Kalibri' transponder," in *Proc. IEEE German Microw. Conf.*, Mar. 2015, pp. 323–326.

[15] J. G. Tang and X. J. Xu, "A new polarimetric active radar calibrator and calibration technique," *Proc. SPIE*, vol. 9643, Oct. 2015, Art. no. 96431U.

[16] D. Rudolf, B. J. Döring, M. Jirousek, J. Reimann, and M. Schwerdt, "A compact antenna rotation concept for precise polarimetric SAR calibration transponders," in *Proc. Eur. Conf. Synth. Aperture Radar*, Berlin, Germany, Jun. 2016, pp. 1–5.

[17] J. Lin, Y. Guo, W. Li, Y. Zhang, and Z. Chen, "Polarimetric calibration based on lexicographic-basis decomposition," *IEEE Geosci. Remote Sens. Lett.*, vol. 13, no. 8, pp. 1149–1152, Aug. 2016.

[18] A. Villa, L. Iannini, D. Giudici, A. Monti-Guarnieri, and S. Tebaldini, "Calibration of SAR polarimetric images by means of a covariance matching approach," *IEEE Trans. Geosci. Remote Sens.*, vol. 53, no. 2, pp. 674–686, Feb. 2015.

[19] R. Touzi, R. K. Hawkins, and S. Cote, "High-precision assessment and calibration of polarimetric RADARSAT-2 SAR using transponder measurements," *IEEE Trans. Geosci. Remote Sens.*, vol. 51, no. 1, pp. 487–503, Jan. 2013.

[20] J. D. Klein, "Calibration of complex polarimetric SAR imagery using backscatter correlations," *IEEE Trans. Aerosp. Electron. Syst.*, vol. 28, no. 1, pp. 183–194, Jan. 1992.

[21] S. Baffelli, O. Frey, C. Werner, and I. Hajnsek, "Polarimetric calibration of the Ku-band advanced polarimetric radar interferometer," *IEEE Trans. Geosci. Remote Sens.*, vol. 56, no. 4, pp. 2295–2311, Apr. 2018.
[22] S. Quegan, "A unified algorithm for phase and cross-talk calibration of polarimetric data-theory and observations," *IEEE Trans. Geosci. Remote Sens.*, vol. 32, no. 1, pp. 89–99, Jan. 1994.
[23] J. J. van Zyl, "Calibration of polarimetric radar images using only image parameters and trihedral corner reflector responses," *IEEE Trans. Geosci. Remote Sens.*, vol. 28, no. 3, pp. 337–348, May 1990.
[24] T. Visentin, J. Hasch, and T. Zwick, "Calibration of a fully polarimetric 8×8 MIMO fmcw radar system at 77 GHz," in *Proc. 11th Eur. Conf. Antennas Propag. (EUCAP)*, Mar. 2017, pp. 2530–2534.
[25] A. Olk, K. Ben Khadhra, and T. Spielmann, "Highly accurate fully-polarimetric radar cross section facility for mono- and bistatic measurements at W-band frequencies," in *Proc. Antenna Meas. Techn. Assoc. Symp. (AMTA)*, Oct. 2017, pp. 1–6.
[26] C. Monzon, "A cross-polarimetric bistatic calibration device for RCS measurements," *IEEE Trans. Antennas Propag.*, vol. 51, no. 4, pp. 937–950, 2003.
[27] C. Beaudoin, T. Horgan, G. Demartinis, M. J. Coulombe, A. J. Gatesman, and W. E. Nixon, "Fully polarimetric bistatic radar calibration with modified dihedral objects," *IEEE Trans. Antennas Propag.*, vol. 66, no. 2, pp. 937–950, Feb. 2018.
[28] M. Pienaar, J. W. Odendaal, J. Joubert, J. E. Cilliers, and J. C. Smit, "Active calibration target for bistatic radar cross-section measurements," *Radio Sci.*, vol. 51, no. 5, pp. 515–523, May 2016.
[29] J. G. Tang, "Polarimetric active radar calibration in target RCS measurement," M.S. thesis, Dept. Elect. Eng., Beihang Univ., Beijing, China, 2016.
[30] B. M. Welsh, L. A. Muth, A. L. Buterbaugh, and B. M. Kent, "Full polarimetric calibration for RCS measurement ranges: Performance analysis and measurement results," in *Proc. Antenna Meas. Techn. Assoc. Symp (AMTA)*, Montreal, QC, Canada, Oct. 1998, pp. 100–105.
[31] N. C. Currie, *Radar Rejectivity Measurements: Techniques and Applications*. Norwood, MA, USA: Artech House, 1989.
[32] J. W. Odendaal and J. Joubert, "Radar cross section measurements using near-field radar imaging," *IEEE Trans. Instrum. Meas.*, vol. 45, no. 6, pp. 948–954, Dec. 1996.
[33] C. A. Balanis, "Aperture antennas," in *Antenna Theory: Analysis and Design*, 3rd ed. Hoboken, NJ, USA: Wiley, 2005.
[34] HFSS. (2017). *Ansoft Corporation*. Canonsburg, PA, USA. Accessed: Feb. 16, 2017. [Online]. Available: http://www.ansys.com/products/electronics/ansys-hfss
[35] FEKO. (2014). *EM Software & Systems-S.A.* Stellenbosch, South Africa. Accessed: Feb. 27, 2015. [Online]. Available: http://www.feko.info
[36] L. Du, H. Liu, Z. Bao, and M. Xing, "Radar HRRP target recognition based on higher order spectra," *IEEE Trans. Signal Process.*, vol. 53, no. 7, pp. 2359–2368, Jul. 2005.
[37] L. A. Muth, "Calibration standards and uncertainties in radar cross section measurements," in *Proc. IEEE Radar Conf. Radar Next Millennium*, Apr. 1999, pp. 326–331.

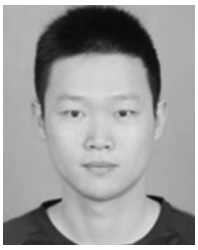

Lingyu Kong was born in Liaoning, China, in 1990. He received the B.S. degree from the School of Physical Science and Technology, Southwest Jiaotong University, Chengdu, China, in 2013. He is currently pursuing the Ph.D. degree in signal and information processing with the School of Electronics and Information Engineering, Beihang University, Beijing, China.

His current research interests include antenna arrays and polarimetric calibration.

Xiaojian Xu was born in Jiangxi, China, in 1963. He received the B.S. degree from the Hefei University of Technology, Hefei, China, in 1983, the M.S. degree from the Beijing Institute of Environmental Features (BIEF), Beijing, China, in 1986, and the Ph.D. degree from the University of Nebraska, Lincoln, NE, USA, in 2002, all in electrical engineering.

He was with the BIEF from 1986 to 1999, where he was mainly involved in research of electromagnetic scattering modeling and microwave imaging. From June 1999 to December 2002, he was with the Environmental Remote Sensing Laboratory, University of Nebraska, where he was involved in the research work on ultrawideband random noise radar, with an emphasis on foliage and ground-penetration applications. Since January 2003, he has been with the School of Electronics and Information Engineering, Beihang University, as a Signal and Information Processing Professor. His current research interests include remote sensing signatures, radar imagery, target recognition, and system modeling.